International Journal of Science & Technology (PRAGYANAM)
Volume 1 • Issue 1 • January–December 2025
ISSN:

# Morphological and Optical Analysis of Tungsten Oxide Nanosheets for Gas Sensing Application

**Tamanna Jindal[1], Peeyush Phogat[2], Shreya[3], Ranjana Jha[4] & Sukhvir Singh[5]**

ABSTRACT

*Tungsten oxide ($WO_3$) is a widely recognized transition metal oxide known for its stability and non-toxicity in nanoparticle form. Its low cost and simple synthesis procedure make it a promising contender for many applications. In the present work, $WO_3$ nanoparticles have been synthesized via a one-step hydrothermal route. X-ray diffraction pattern demonstrated the formation of a single phase of high crystallinity tungsten trioxide. Crystallite size and strain were used to explain the structural defects and formation mechanism of $WO_3$. UV-visible spectroscopy was used to investigate the optical characteristics, and the single phases of $WO_3$ showed a band gap of 2.5 eV. Field Emission Scanning electron microscope (FESEM) images demonstrated the morphological properties of material. As a result, tungsten trioxide was found to be more environmentally sensitive than pre-transition-metal oxides.*

**Keywords:** Tungsten Oxide, Nanomaterial, Nanosheets, Hydrothermal

## INTRODUCTION

The general consensus around nanoparticles and nanotechnology has been evolving over the previous few years, and the position may have changed. The current work focuses on tungsten oxide which is well-known metal for gas sensing applications. It has exceptional optical features, specifically the ability to change colour depending on its oxidation state [1]. This feature has led to its employment in a variety of sectors and gained attention across various research domains due to its versatility in electrochromic devices (such as displays and smart screens), where its transparency can change in response to an applied voltage, as well as in energy storage, catalysis and gas sensing. [2], [3], [4].

Over the past 15 years, the adaptable nature of $WO_3$ has led to its utilization in a range of applications [5]. Research into photoelectrochemical cells for water splitting began in 1976, and more recent studies have investigated their potential application in dye-sensitized solar cells, batteries, and sensor technology [6]. Moreover, $WO_3$ has gathered significant interest for sensing applications due to its role as a prominent n-type gas-sensing material, proving instrumental in detecting various hazardous gases [7].

The structural characteristics and gas-sensing behaviour of nanocrystalline $WO_3$ powders synthesized through a sol-gel process using tungstic acid [8]. A comparative study of electrochromic tungsten oxide films prepared via spin-coating and dip-coating techniques, evaluating their structural, morphological, optical, and electrochemical properties [9, 10]. Still, there remains a significant research gap concerning the tungsten oxide for gas sensing purposes [11], [12].

[1] Research Lab for Energy System, Department of Physics, Netaji Subhas University of Technology, New Delhi, India.
E-mail: tamannajindal3@gmail.com

[2] Research Lab for Energy System, Department of Physics, Netaji Subhas University of Technology, New Delhi, India.
E-mail: peeyush.phogat@gmail.com

[3] Research Lab for Energy System, Department of Physics, Netaji Subhas University of Technology, New Delhi, India.
E-mail: shreyasharma.aug15@gmail.com

[4] Research Lab for Energy System, Department of Physics, Netaji Subhas University of Technology, New Delhi, India.
E-mail: drranjanajha@gmail.com

[5] Research Lab for Energy System, Department of Physics, Netaji Subhas University of Technology, New Delhi, India.
E-mail: sukhvirster@gmail.com

Extensive research has been conducted on tungsten oxide nanoparticles and their flat structures, such as 2D nanosheets or thin films, primarily due to their remarkable surface area-to-volume ratio. Two-dimensional nanosheets, owing to their substantial surface area and relatively small volume, are particularly well-suited for gas sensing applications [13], [14]. Various methods, including sol-gel synthesis, hydrothermal approaches, and chemical vapor deposition, can be employed to produced nanostructured $WO_3$ materials [15], [16], [17].

Tungsten oxide has been extensively researched for its ability to transition reversibly between a colourless state and a blue colour when subjected to alternating small positive and negative voltages [18], [19]. The stoichiometry of $WO_3$ can change significantly, causing oxygen vacancies to occur in its crystal structure [20]. These vacancies can have an effect on its electrical and electrochemical characteristics and are useful in some applications like gas sensing, photodetectors, solar cells, etc. Hydrated versions of $WO_3$ exist, such as $HxWO_3$ (where x is a variable) [21]. These hydrates can have unique properties and are useful in applications such as gas detection [22], [23].

Recently, there has been significant interest in tungsten-oxide-based materials due to their capability to absorb near-infrared (NIR) [24], [25], [26] light effectively and their efficient conversion of light into heat. Moreover, these materials possess an intriguing oxygen defect structure and exhibit strong local surface plasma resonance (LSPR) [27], [28], [29] resulting in robust photo absorption across a broad range of NIR wavelengths. Previously, a range of light-absorbing nanomaterials, including noble metals, polymeric materials, and other inorganic nanomaterials, have been investigated for their potential use in photothermal therapy for cancer treatment [30].

Even $WO_3$ has been utilized as an anode material due to its high theoretical capacity, low cost, and environmentally friendly nature [31]. Its main limitation, however, lies in its low electrical conductivity, a challenge that has been addressed with $WO_3$−x materials. The research focused on the development of high-performance mesoporous $WO_3$−x anodes using a hard template approach to enhance electrical conductivity. The resulting material exhibited an impressive reversible capacity of 748 mAh $g^{-1}$ and a high volumetric capacity of 1,500 mAh $cm^{-3}$ compared to bulk $WO_3$−x.

In recent years, the quest for efficient gas sensing materials has intensified due to their crucial role in various industrial [32], environmental [33], and biomedical applications [34]. Among the myriad of materials explored, tungsten oxide ($WO_3$) has emerged as a promising candidate owing to its unique properties such as high surface area, excellent chemical stability, and sensitivity to various gas species [35],[36].

Nanoscale morphological and optical properties play a significant role in determining the performance of gas sensing materials [37], [38]. Tungsten oxide nanosheets, with their two-dimensional structure, offer a large surface-to-volume ratio and enhanced gas interaction capabilities, making them particularly attractive for gas sensing applications [39], [40].

This paper presents a comprehensive study on the morphological and optical characteristics of tungsten oxide nanosheets and their implications for gas sensing. We investigate the synthesis methods, and examine the structural properties, surface morphology [41], and optical properties of $WO_3$ nanosheets using various analytical techniques such as XRD, UV-Visible spectroscopy and FESEM [42], [43].

The novelty of this study lies in its exploration of an unaddressed research gap, specifically analysed the morphological and optical properties of the synthesized material [44]. Nanoparticles of $WO_3$ doped materials were synthesized using the hydrothermal method and subsequently evaluated for their potential application in gas sensors. The orthorhombic structure of $WO_3$ has been presented in Fig. 1.

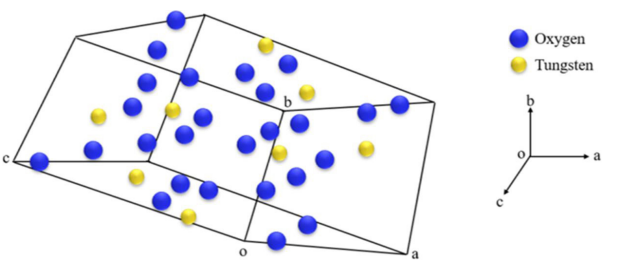


**Fig. 1.** 3D model of orthorhombic $WO_3$

## EXPERIMENTAL SECTION

### Chemical Reagents

During the synthesis process, analytical reagent (AR) grade chemicals and reagents (as detailed in Table

1) were used without further purification. Absolute ethanol and deionized (DI) water were employed for cleaning and washing procedures. Unless otherwise stated, all solutions were prepared using DI water.

**Table 1.** Chemicals utilized in the synthesis process

| *Chemical Name* | *Chemical Formula* | *Manufacturing Company* | *Purity* |
|---|---|---|---|
| Sodium Tungstate | $Na_2WO_4$ | M/s Thomas Baker | 98% |
| Oxalic Acid | $HO_2C{=}CO_2H$ | M/s Loba Chemie | 99% |
| Nitric Acid | $HNO_3$ | M/s CDH Ltd | 98% |

### Synthesis

The single-step hydrothermal method was employed to synthesize tungsten oxide nanosheets. To prepare a single phase of $WO_3$, a solution of $Na_2WO_4$ (0.096 M) was initially prepared in 30 ml DI water and stirred for 15 minutes Afterwards, the mixture was agitated for a few minutes with the addition of 5ml $HNO_3$. A 0.249 M solution of oxalic acid was prepared in 20 mL of deionized (DI) water and stirred for 30 minutes. This solution was then added dropwise to the pre-prepared solution under continuous stirring. The resulting mixture was stirred further for one hour at room temperature. Subsequently, the precursor solution was transferred into a Teflon-lined hydrothermal autoclave reactor and heated to 220°C for 24 hours in a hot air oven. It was then left overnight to cool naturally. The solution was later centrifuged and washed with DI water and ethanol several times. Finally, the precipitates were collected and dried in a vacuum oven at 60°C. The sample was then grounded to obtained the nanoparticles of $WO_3$. The powder was then calcinated in the presence of oxygen for an hour at 500°C with a heating rate of 1°/min.

## RESULTS AND DISCUSSON

### X-Ray Diffraction

The XRD pattern of the synthesized powder sample was recorded within the 2θ range of 10° to 80°. This technique is used to characterize the structural properties of materials, including tungsten oxide ($WO_3$) nanosheets, which are essential for understanding their behaviour in gas sensing applications [45], [46].

XRD involves bombarding a sample with X-rays and measuring the intensity and angle of the diffracted X-rays. This data provides information about the crystal structure, phase composition, lattice parameters, and crystallinity of the material [47].

For our study on the morphological and optical analysis of tungsten oxide nanosheets, XRD serves as a crucial characterization technique. By analysing the diffraction patterns obtained from $WO_3$ nanosheets, we can identify the crystal phases present, assess their purity, and determine their crystalline structure.

The peaks of the synthesized sample were analysed and indexed using the JCPDS file 01-071-0131, showing a good match with $WO_3$. The synthesized $WO_3$ exhibited an orthorhombic crystal structure corresponding to specific (hkl) planes. given as (002), (020), (200), (120), (112), (220), (122), (222), (004), (040), (140), (420), (432), (440) and (160) as shown in Fig. 2.

The JCPDS file specifies that crystal structure of $WO_3$ as being in the space group Pmnb which means that $WO_3$ crystal structure has an orthorhombic symmetry with specific translational and rotational elements [48].

The Pmnb space group specifies the following symmetry elements, where 'P' defines a primitive lattice, 'm' represents the Mirror planes perpendicular to the a-axis, 'n' defines the Mirror planes perpendicular to the b-axis and 'b' illustrates the Glide planes perpendicular to the c-axis. In $WO_3$, tungsten atoms are located at the corners and edges of distorted octahedra formed by oxygen atoms. Each tungsten atom is surrounded by six oxygen atoms, and each oxygen atom is shared between two octahedra [49].

This arrangement results in an orthorhombic crystal structure where the lattice parameters are unequal. Typically, in $WO_3$, the lattice parameters are $a \neq b \neq c$, and the angles between the lattice vectors are 90°.

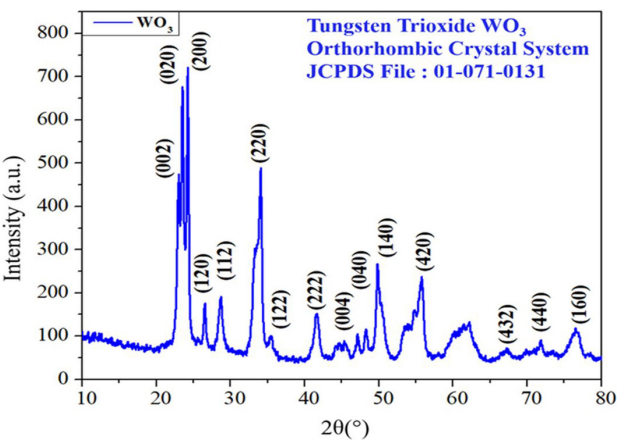


**Fig. 2.** XRD pattern of $WO_3$

### Lattce Parameters, Crystallite Size and Strain

Lattice parameters are the lengths of the edges and the angles between them that define the unit cell of a crystal lattice. In other words, they describe the geometric arrangement of atoms in a crystal structure.

The crystallite size corresponds to the size of the smallest crystal in, a single crystal in powder form. Debye Scherrer formula provided in equation-1 has often been used to determine the size of crystallites. The Debye Scherrer formula is given as,

$$d = K\frac{\lambda}{\beta\cos\theta} \quad ...(1)$$

Here, d represents the average diameter of crystallite, value of shape constant (k) is 0.9, λ stands for radiation wavelength (1.54 Å), β refers to full width at half maxima (FWHM), θ is Bragg's angle of respective peaks [50], [51]. The average of analysed peaks was determined and the obtained crystallite size of $WO_3$ was approx. 23 nm. This signifies the average size of individual crystalline domains. Smaller crystallite sizes can enhance surface area, potentially improving reactivity or electrical properties, particularly in catalysis or semiconductor applications [52], [53]. The lattice parameters for as synthesized sample were calculated using the equation-2.

$$\frac{1}{d^2} = \frac{h^2}{a^2} + \frac{k^2}{b^2} + \frac{l^2}{c^2} \quad ...(2)$$

The inter planer spacing is denoted by d, with (hkl) representing the Miller indices, while a, b, and c correspond to the lattice sides. Table 2 illustrates the differences between the lattice parameters from the JCPDS file and the calculated values.

**Table 2.** Lattice parameters of the as-synthesized sample

| *Parameters* | *Calculated Value for $WO_3$* | *JCPDS Value for $WO_3$* |
|---|---|---|
| a (Å) | 7.37 | 7.34 |
| b (Å) | 7.57 | 7.57 |
| c (Å) | 7.34 | 7.75 |

The deviated value of lattice parameter represents the presence of micro strain. The Williamson Hall (W-H) Plot which is a graphical tool commonly used to calculate the strain and crystallite size, for describing the microstructural characteristics of crystalline materials and which applied the following equation,

$$\beta\cos\theta = (\varepsilon \times 4\sin\theta) + K\lambda / D \quad ...(3)$$

Here, ε indicates the micro strain in the as synthesised material [54], [55]. The W-H plot is in between (4 sin θ) and (β cos θ), for $WO_3$ the slope and intercept are 0.00325 and 0.00301 respectively observed, as shown in Fig. 3(a). The crystallite size and strain obtained by using the W-H Plot is 46.04 nm and 0.00325 respectively.

The Size Strain (S-S) plot is also used as it offers precise and unbiased measurements of crystallite size and strain [56]. S-S plot accounts for multiple transitions in the material, including direct and indirect transitions, while the W-H plot typically assumes a single type of transition [57], [58].

The S-S plot often yields a more linear relationship between the absorption coefficient squared ($\alpha^2$) and the photon energy and even requires less data processing. The equation 4 is the formula that was applied [59].

$$(d\beta\cos\theta)^2 = K\lambda/D\,(d^2\beta\cos\theta) + \varepsilon^2/4 \quad ...(4)$$

The S-S plot was obtained between ($d^2\beta\cos\theta$) and ($d\beta\cos\theta)^2$ using which the slope is 0.00698 and intercept equals to -1.31905E-7 as observed in Fig. 3(b). The crystallite size and strain calculated by S-S Plot are 19.85 nm and 0.00229 respectively.

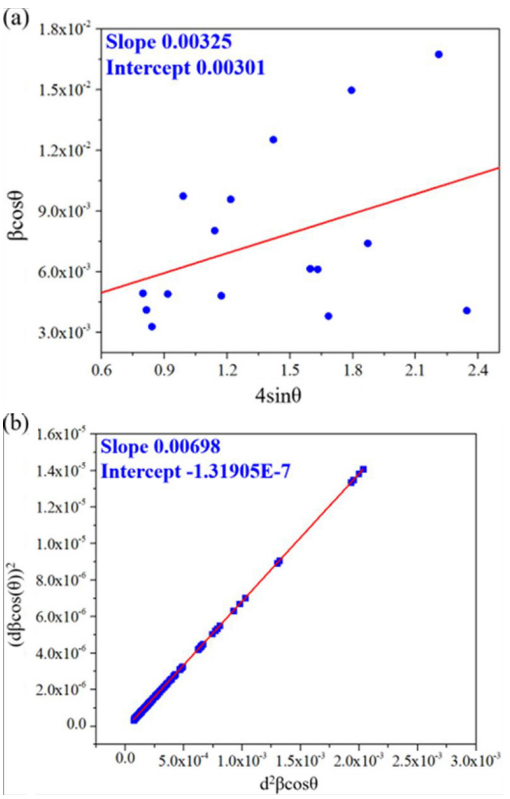


**Fig. 3.** (a) W-H plot of the synthesized sample, (b) S-S plot of the prepared sample

**UV-Visble Spectroscopy**

Ultraviolet-visible spectroscopy, is a widely used analytical technique to study the electronic transitions that occur in molecules.

UV-Vis spectroscopy detects the absorption of ultraviolet (UV) or visible light by molecules. When molecules absorb UV or visible light, their electrons transition from lower energy states to higher ones [60]. The difference in energy between these states matches the absorbed light's energy, appearing as absorption bands in the UV-Vis spectrum.

This technique was employed for as synthesized sample with wavelength ranging from 190 to 850 nm. The maximum absorption peaks were seen in the UV region between 190 nm and 450 nm.

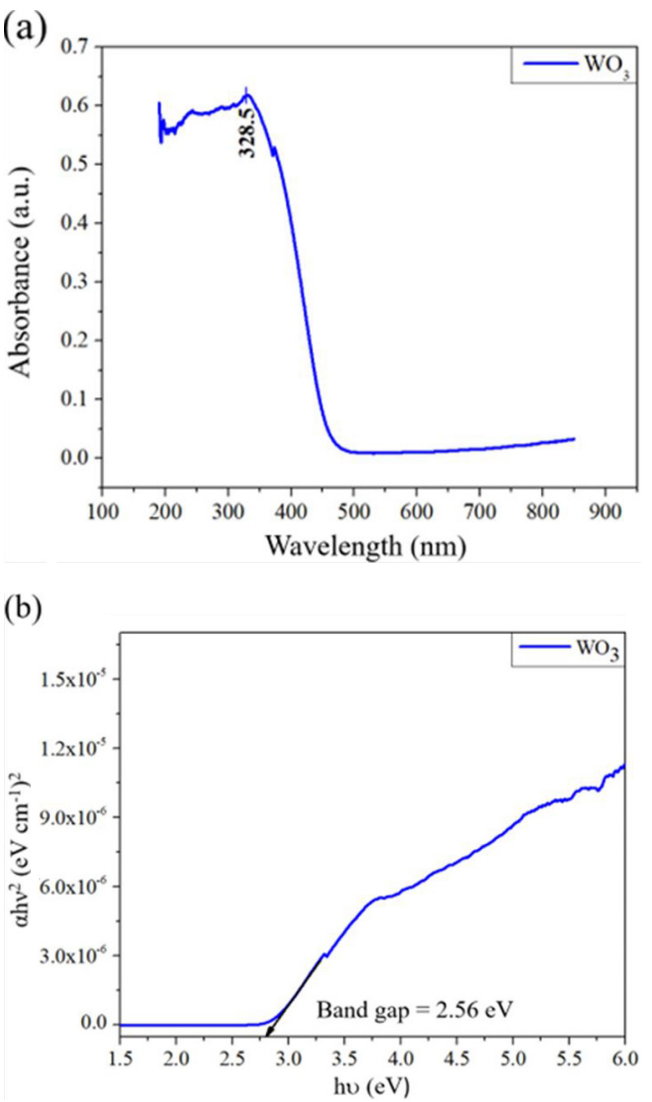


**Fig. 4.** (a) Absorption spectra of $WO_3$, (b) Tauc Plot of the synthesized sample

In the UV region, molecules undergo electronic transitions, where electrons are excited from lower energy levels to higher ones. This transition results in absorption of UV light, leading to characteristic absorption spectra [61]. For as synthesized material, 328.5 was the highest absorption peak as shown in Fig. 4(a).

UV analysis represents the optical bandgap, for which we employed the Tauc plot [62], [63]. Tauc plot defines the bandgap energy (Eg) of a material. The Tauc plot is a graphical representation of a semiconductor material's absorption edge, typically plotted against specific parameters, $(\alpha h\nu)^2$ versus the photon energy ($h\nu$). The equation used for this,

$$\alpha h\nu = \mathrm{A}[h\nu - Eg]^{1/n} \quad ...(5)$$

Here, $\alpha$ denotes the absorption coefficient, $A$ is proportionality constant, $E_g$ represents the bandgap and the nature of transition represented by $n$ exponent. Using this formula, the bandgap of $WO_3$ was determined to be 2.56 eV, as shown in the Fig. 4(b). The bandgap of 2.56 eV was optimum for a number of applications [64], [65].

In the optoelectronic devices like photodetectors and sensors, the bandgap may provide a suitable balance between their sensitivity to visible light and electrical conductivity [66].

The refractive index is a helpful parameter for characterising and identifying compounds. It determines how light propagates through a material. It affects phenomena such as reflection, refraction, and dispersion. Understanding the refractive index is crucial for designing optical components like lenses, prisms, and fibres. Refractive index can serve as a characteristic property for identifying materials. Different substances have distinct refractive indices, allowing for their identification through techniques like refractometry or ellipsometry.

The effective refractive index of a medium can vary when a gas with a different refractive index than the medium in the vicinity interacts with it [67], [68], [69]. The variation of refractive index can detect the presence of specific gas and used for gas sensors. The material's Refractive Index is also calculated using the equation-6.

$$\frac{n^2-1}{n^2+2} = 1 - \sqrt{E_g / 20} \quad ...(6)$$

Here, $n$ denotes the refractive index, while $E_g$ represents the corresponding band gap of the sample [70]. As determined earlier the band gap of $WO_3$ is 2.56 eV, the as synthesized material $WO_3$ has a refractive index of 2.53.

**Morphological Analysis**

FESEM (Field-Emission Scanning Electron Microscopy) characterization involves using a high-resolution electron microscope to examine the surface morphology and structure of materials at the nanoscale [71]. It provides detailed images of the sample's surface, revealing features such as size, shape, and distribution of particles or structures [72].

FESEM images can also reveal surface features such as roughness, porosity, and the presence of defects or crystalline facets [73]. These surface characteristics can influence the material's properties and applications.

The image can indicate whether the $WO_3$ nanoparticles are well-dispersed or aggregated. Aggregation can affect the material's properties, such as its reactivity and optical behaviour [74]. Depending on the imaging conditions and the quality of the sample, FESEM images may provide insights into the crystalline structure of $WO_3$. This can be further confirmed by complementary techniques such as X-ray diffraction (XRD).

FESEM technique provides a significant experimental approach used for studying the surface properties and composition of materials at the microscopic level. Depending on the synthesis approach and conditions employed, $WO_3$ can have a variety of morphologies [75].

The nanoflower like morphology can be seen through hydrothermal route but during this process metal oxides may contain the volatile impurities such as water, which indicated the presence of acidic environment and promotes the nucleation and growth. To remove these volatile elements the calcination process is frequently used [76]. The calcination transforms the morphology of tungsten trioxide into the 2D Nanosheets. These tend to be thin, flat constructions with a high aspect ratio, resembling paper sheets within range of 100 nm as shown in Fig. 5(a).

Energy Dispersive X-ray Spectroscopy (EDX) spectra provide information about the elemental composition of a sample [77]. When a material is exposed to high-energy electrons or X-rays, it emits characteristic X-rays with energy levels that correspond to the specific elements within the sample. It identifies the elements present in the sample by detecting characteristic X-rays emitted when the electrons of atoms in the sample are

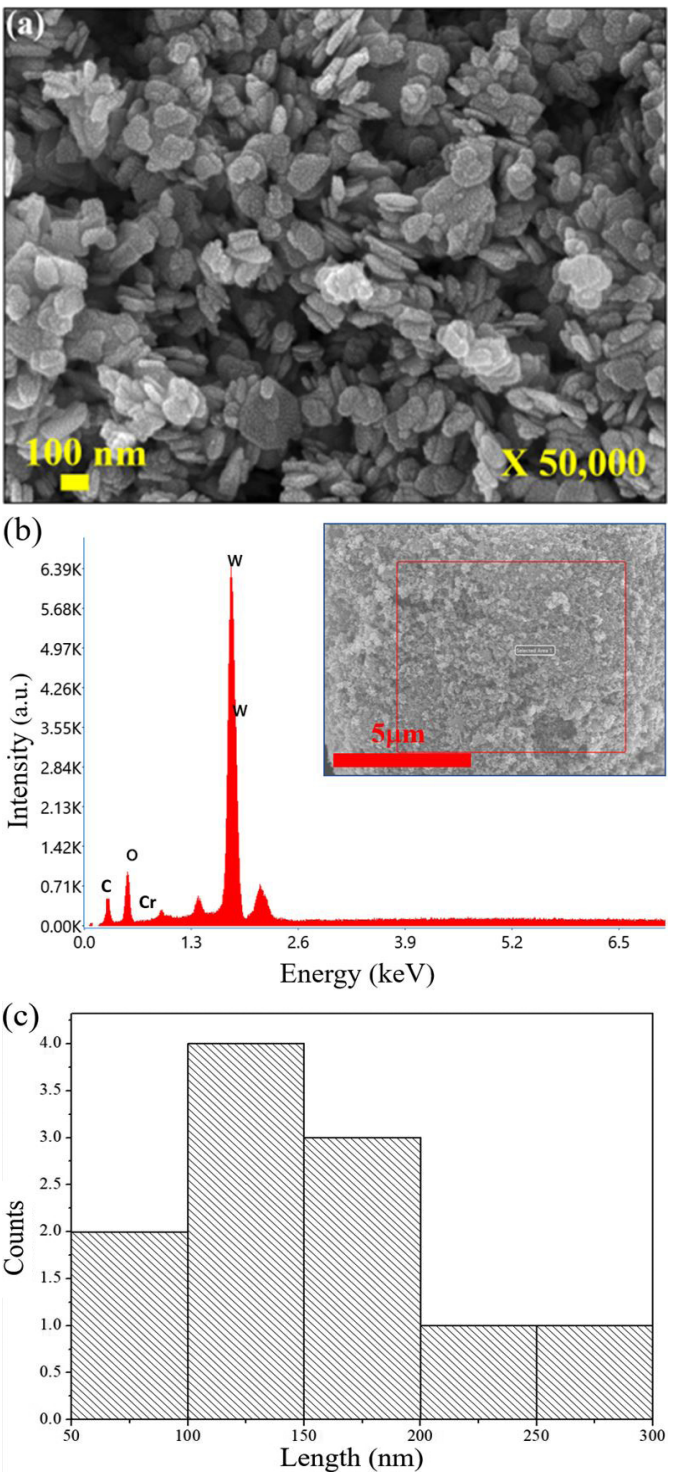


**Fig. 5.** (a) FESEM Image of the tungsten oxide, (b) EDX Spectra of corresponding area, (c) Particle Size Distribution

excited and transition to lower energy levels [78]. It gives an indication of the relative abundance of each element in the sample by measuring the intensity of the characteristic X-rays emitted.

In conjunction with field emission scanning electron microscopy (FESEM), EDX can provide information on the spatial distribution of elements, showing where specific elements are concentrated in the sample [79].

Fig. 5(b) shows that the tungsten (W) and oxygen (O) are present in the sample. Furthermore, the sample contains a particularly high concentration of tungsten. The signals attributed to carbon and copper in the EDX spectra originated from the carbon coating on the copper grid of electron microscope.

The observed nanosheets exhibited particle sizes ranging from 100 nm to 150 nm, as illustrated in Fig. 5(c). Their high aspect ratio contributed to enhanced material reactivity. They are hexagonal, rectangular 2D shape nanosheets. Even 2D $WO_3$ nanosheets frequently have outstanding structural and optical characteristics, making them valuable for sensors and photocatalysis.

## CONCLUSION

The current work emphasis on the structural and optical study of $WO_3$ for application in gas sensors. The synthesis process used for $WO_3$ was the hydrothermal method. XRD analysis of the as-synthesized powder sample revealed that the material's crystal structure has orthorhombic symmetry. The formation of 2D nanosheets demonstrated by the FESEM technique. The band gap obtained from the tauc plot is 2.56 eV, within the region of wide bandgap semiconductors with a refractive index of 2.53. The Debye-Scherrer method yielded a crystallite size of 23.15 nm. The crystallite size and strain values calculated from the W-H Plot were 46.04 nm and 0.00325, respectively. Whereas, the S-S plot showed crystallite size and strain of 19.85 nm and 0.00229, respectively. Because of its varied qualities, $WO_3$ can be applied to a wide range of situations. $WO_3$ is widely explored for photocatalytic properties and has been proved useful for environmental cleanup and water splitting for the production of hydrogen. $WO_3$ has also been explored for gas sensing applications. When exposed to reducing gases, such as hydrogen, its broad bandgap allows the generation of charge carriers in the crystal lattice, or oxygen vacancies in the crystal lattice when exposed to oxidizing gases like ozone. It can therefore be utilised in gas sensors to identify different gases, such as hydrogen, ozone ($O_3$) and nitrogen dioxide ($NO_2$). Thus, the future prospect is to use the as-synthesized $WO_3$ nanosheets for gas sensing applications due to its high aspect ratio and advantageous band gap.

## ACKNOWLEDGMENT

The authors would like to express their gratitude to the Vice Chancellor of NSUT, Prof. Anand Srivastava, for his financial support.

## REFERENCES

[1] H. Pakdel et al., "Synthesis of $WO_3$ nanopowder using a green surfactant for efficient gas sensing applications," *Ceram Int*, vol. 49, no. 18, pp. 30501–30509, Sep. 2023, doi: 10.1016/J.CERAMINT.2023.06.314.

[2] A. Hoel, L.F. Reyes, P. Heszler, V. Lantto, and C. G. Granqvist, "Nanomaterials for environmental applications: Novel $WO_3$-based gas sensors made by advanced gas deposition," *Current Applied Physics*, vol. 4, no. 5, pp. 547–553, Aug. 2004, doi: 10.1016/J.CAP.2004.01.016.

[3] H. Su et al., "Nanomaterial-based biosensors for biological detections," *Adv Health Care Technol*, vol. 3, pp. 19–29, Oct. 2017, doi: 10.2147/AHCT.S94025.

[4] J.S. Meena, S. Bin Choi, S.-B. Jung, and J.-W. Kim, "Advances in Silver Nanowires-Based Composite Electrodes: Materials Processing, Fabrication, and Applications," *Adv Mater Technol*, vol. 8, no. 19, p. 2300602, 2023, doi: https://doi.org/10.1002/admt.202300602.

[5] Y. Zhu, Y. Deng, P. Yi, L. Peng, X. Lai, and Z. Lin, "Flexible Transparent Electrodes Based on Silver Nanowires: Material Synthesis, Fabrication, Performance, and Applications," *Advanced Materials Technologies*, vol. 4, no. 10. Wiley-Blackwell, Oct. 01, 2019. doi: 10.1002/admt.201900413.

[6] Y. Zhang, P. He, M. Luo, X. Xu, G. Dai, and J. Yang, "Highly stretchable polymer/silver nanowires composite sensor for human health monitoring," *Nano Res*, vol. 13, no. 4, pp. 919–926, 2020, doi: 10.1007/s12274-020-2730-z.

[7] A. Elzwawy, A.M. Mansour, H.S. Magar, A.B.A. Hammad, R.Y.A. Hassan, and A.M. El Nahrawy, "Exploring the structural and electrochemical sensing of wide bandgap calcium phosphate/CuxFe3-xO4 core-shell nanoceramics for H2O2 detection," *Mater Today Commun*, vol. 33, Dec. 2022, doi: 10.1016/j.mtcomm.2022.104574.

[8] I. Jiménez, J. Arbiol, A. Cornet, and J.R. Morante, "Structural and gas-sensing properties of $WO_3$ nanocrystalline powders obtained by a sol-gel method from tungstic acid," *IEEE Sens J*, vol. 2, no. 4, pp. 329–334, 2002, doi: 10.1109/JSEN.2002.803747.

[9] M. Deepa, T.K. Saxena, D.P. Singh, K.N. Sood, and S.A. Agnihotry, "Spin coated versus dip coated electrochromic tungsten oxide films: Structure, morphology, optical and electrochemical properties," *Electrochim Acta*, vol. 51, no. 10, pp. 1974–1989, Feb. 2006, doi: 10.1016/j.electacta.2005.06.027.

[10] G. Adilakshmi, A. Sivasankar Reddy, P. Sreedhara Reddy, and C. Seshendra Reddy, "Electron beam evaporated nanostructure $WO_3$ films for gas sensor application," *Materials Science and Engineering: B*, vol. 273, Nov. 2021, doi: 10.1016/j.mseb.2021.115421.

[11] Shreya, P. Phogat, R. Jha, and S. Singh, "Microwave-synthesized γ-$WO_3$ nanorods exhibiting high current density and diffusion characteristics," *Transition Metal Chemistry*, vol. 48, no. 3, pp. 167–183, Jun. 2023, doi: 10.1007/S11243-023-00533-Y.

[12] P. Van Tong, N.D. Hoa, N. Van Duy, D.T.T. Le, and N. Van Hieu, "Enhancement of gas-sensing characteristics of hydrothermally synthesized $WO_3$ nanorods by surface decoration with Pd nanoparticles," *Sens Actuators B Chem*, vol. 223, pp. 453–460, Feb. 2016, doi: 10.1016/J.SNB.2015.09.108.

[13] P. Phogat, Shreya, R. Jha, and S. Singh, "Optical and Microstructural Study of Wide Band Gap ZnO@ ZnS Core–Shell Nanorods to be Used as Solar Cell Applications," pp. 419–429, 2023, doi: 10.1007/978-981-99-2349-6_38.

[14] X. Fang et al., "ZnS nanostructures: From synthesis to applications," *Prog Mater Sci*, vol. 56, no. 2, pp. 175–287, Feb. 2011, doi: 10.1016/J.PMATSCI.2010.10.001.

[15] B. Deepa and V. Rajendran, "Pure and Cu metal doped $WO_3$ prepared via co-precipitation method and studies on their structural, morphological, electrochemical and optical properties," *Nano-Structures and Nano-Objects*, vol. 16, pp. 185–192, Oct. 2018, doi: 10.1016/j.nanoso.2018.06.005.

[16] S. Sharma, P. Phogat, R. Jha, and S. Singh, "Electrochemical and Optical Properties of Microwave Assisted MoS2 Nanospheres for Solar Cell Application," *International Journal of Smart Grid and Clean Energy*, pp. 66–72, 2023, doi: 10.12720/SGCE.12.3.66-72.

[17] S. Mohammed Harshulkhan, K. Janaki, G. Velraj, R. Sakthi Ganapthy, and M. Nagarajan, "Effect of Ag doping on structural, optical and photocatalytic activity of tungsten oxide ($WO_3$) nanoparticles," *Journal of Materials Science: Materials in Electronics*, vol. 27, no. 5, pp. 4744–4751, May 2016, doi: 10.1007/S10854-016-4354-3/FIGURES/9.

[18] R. Sivakumar, R. Gopalakrishnan, M. Jayachandran, and C. Sanjeeviraja, "Investigation of x-ray photoelectron spectroscopic (XPS), cyclic voltammetric analyses of $WO_3$ films and their electrochromic response in FTO/$WO_3$/electrolyte/FTO cells," *Smart Mater Struct*, vol. 15, no. 3, pp. 877–888, Jun. 2006, doi: 10.1088/0964-1726/15/3/025.

[19] Z. Xie et al., "Fast fabrication of a $WO_3 \cdot 2H_2O$ thin film with improved electrochromic properties," *J Mater Chem*, vol. 22, no. 37, pp. 19904–19910, Oct. 2012, doi: 10.1039/c2jm33622g.

[20] J. Dahiya, P. Phogat, A. Hooda, and S. Khasa, "Investigations of Praseodymium doped LiF-ZnO-Bi2O3-B2O3 glass matrix for photonic applications," Jan. 2024, p. 20065. doi: 10.1063/5.0178197.

[21] M. Arshad et al., "Synthesis and characterization of Zn doped $WO_3$ nanoparticles: Photocatalytic, antifungal and antibacterial activities evaluation," *Mater Res Express*, vol. 7, no. 1, 2020, doi: 10.1088/2053-1591/ab6380.

[22] H. Song et al., "Synthesis of Fe-doped $WO_3$ nanostructures with high visible-light-driven photocatalytic activities," *Appl Catal B*, vol. 166–167, pp. 112–120, May 2015, doi: 10.1016/j.apcatb.2014.11.020.

[23] T. Tesfamichael, A. Ponzoni, M. Ahsan, and G. Faglia, "Gas sensing characteristics of Fe-doped tungsten oxide thin films," *Sens Actuators B Chem*, vol. 168, pp. 345–353, Jun. 2012, doi: 10.1016/j.snb.2012.04.032.

[24] Z. Lv, S. He, Y. Wang, and X. Zhu, "Noble Metal Nanomaterials for NIR-Triggered Photothermal Therapy in Cancer," *Adv Healthc Mater*, vol. 10, no. 6, p. 2001806, 2021, doi: https://doi.org/10.1002/adhm.202001806.

[25] S. Jiang, J. Lin, and P. Huang, "Nanomaterials for NIR-II Photoacoustic Imaging," *Adv Healthc Mater*, vol. 12, no. 16, p. 2202208, 2023, doi: https://doi.org/10.1002/adhm.202202208.

[26] S. Zeng, D. Baillargeat, H.-P. Ho, and K.-T. Yong, "Nanomaterials enhanced surface plasmon resonance for biological and chemical sensing applications," *Chem. Soc. Rev.*, vol. 43, no. 10, pp. 3426–3452, 2014, doi: 10.1039/C3CS60479A.

[27] A. Bonyár, "Label-Free Nucleic Acid Biosensing Using Nanomaterial-Based Localized Surface Plasmon Resonance Imaging: A Review," *ACS Appl Nano Mater*, vol. 3, no. 9, pp. 8506–8521, Sep. 2020, doi: 10.1021/acsanm.0c01457.

[28] S. Lee, H. Song, H. Ahn, S. Kim, J. Choi, and K. Kim, "Fiber-Optic Localized Surface Plasmon Resonance Sensors Based on Nanomaterials," *Sensors*, vol. 21, no. 3, 2021, doi: 10.3390/s21030819.

[29] P. Pei et al., "X-ray-activated persistent luminescence nanomaterials for NIR-II imaging," *Nat Nanotechnol*,

vol. 16, no. 9, pp. 1011–1018, 2021, doi: 10.1038/s41565-021-00922-3.

[30] Z. Bao, X. Liu, Y. Liu, H. Liu, and K. Zhao, "Near-infrared light-responsive inorganic nanomaterials for photothermal therapy," *Asian J Pharm Sci*, vol. 11, no. 3, pp. 349–364, 2016, doi: https://doi.org/10.1016/j.ajps.2015.11.123.

[31] A. Tacca et al., "Photoanodes Based on Nanostructured $WO_3$ for Water Splitting," *ChemPhysChem*, vol. 13, no. 12, pp. 3025–3034, 2012, doi: https://doi.org/10.1002/cphc.201200069.

[32] S. Adhikari, K. Sarath Chandra, D.-H. Kim, G. Madras, and D. Sarkar, "Understanding the morphological effects of $WO_3$ photocatalysts for the degradation of organic pollutants," *Advanced Powder Technology*, vol. 29, no. 7, pp. 1591–1600, 2018, doi: https://doi.org/10.1016/j.apt.2018.03.024.

[33] N. Naseri, R. Azimirad, O. Akhavan, and A.Z. Moshfegh, "Improved electrochromical properties of sol–gel $WO_3$ thin films by doping gold nanocrystals," *Thin Solid Films*, vol. 518, no. 8, pp. 2250–2257, 2010, doi: https://doi.org/10.1016/j.tsf.2009.08.001.

[34] L. Santos et al., "Synthesis of $WO_3$ nanoparticles for biosensing applications," *Sens Actuators B Chem*, vol. 223, pp. 186–194, 2016, doi: https://doi.org/10.1016/j.snb.2015.09.046.

[35] X. Mu et al., "High efficiency organic/silicon hybrid solar cells with doping-free selective emitter structure induced by a $WO_3$ thin interlayer," *Nano Energy*, vol. 16, pp. 54–61, 2015, doi: https://doi.org/10.1016/j.nanoen.2015.06.015.

[36] S. Ansari, M.S. Ansari, S.P. Satsangee, and R. Jain, "$WO_3$ decorated graphene nanocomposite based electrochemical sensor: A prospect for the detection of anti-anginal drug," *Anal Chim Acta*, vol. 1046, pp. 99–109, 2019, doi: https://doi.org/10.1016/j.aca.2018.09.028.

[37] J. Ma et al., "Pt Nanoparticles Sensitized Ordered Mesoporous $WO_3$ Semiconductor: Gas Sensing Performance and Mechanism Study," *Adv Funct Mater*, vol. 28, no. 6, p. 1705268, 2018, doi: https://doi.org/10.1002/adfm.201705268.

[38] C. Wang et al., "Hierarchical flower-like $WO_3$ nanostructures and their gas sensing properties," *Sens Actuators B Chem*, vol. 204, pp. 224–230, 2014, doi: https://doi.org/10.1016/j.snb.2014.07.083.

[39] B. Behera and S. Chandra, "Synthesis of $WO_3$ nanorods by thermal oxidation technique for $NO_2$ gas sensing application," *Mater Sci Semicond Process*, vol. 86, pp. 79–84, 2018, doi: https://doi.org/10.1016/j.mssp.2018.06.022.

[40] A. Staerz, S. Somacescu, M. Epifani, T. Kida, U. Weimar, and N. Barsan, "$WO_3$-Based Gas Sensors: Identifying Inherent Qualities and Understanding the Sensing Mechanism," *ACS Sens*, vol. 5, no. 6, pp. 1624–1633, Jun. 2020, doi: 10.1021/acssensors.0c00113.

[41] P.V. Karthik Yadav, B. Ajitha, Y.A.K. Reddy, V.R. Minnam Reddy, M. Reddeppa, and M.-D. Kim, "Effect of sputter pressure on UV photodetector performance of $WO_3$ thin films," *Appl Surf Sci*, vol. 536, p. 147947, 2021, doi: https://doi.org/10.1016/j.apsusc.2020.147947.

[42] M. Jamali and F. Shariatmadar Tehrani, "Thermally stable $WO_3$ nanostructure synthesized by hydrothermal method without using surfactant," *Materials Science and Engineering: B*, vol. 270, p. 115221, 2021, doi: https://doi.org/10.1016/j.mseb.2021.115221.

[43] A.S. Hammad, H.M. El-Bery, A.H. EL-Shazly, and M. F. Elkady, "Effect of $WO_3$ Morphological Structure on its Photoelectrochemical Properties," *Int J Electrochem Sci*, vol. 13, no. 1, pp. 362–372, 2018, doi: https://doi.org/10.20964/2018.01.32.

[44] K. Thiyagarajan, M. Muralidharan, and K. Sivakumar, "Defects Induced Magnetism in $WO_3$ and Reduced Graphene Oxide-$WO_3$ Nanocomposites," *J Supercond Nov Magn*, vol. 31, no. 1, pp. 117–125, Jan. 2018, doi: 10.1007/s10948-017-4184-4.

[45] S. Aksay, "Effects of Al dopant on XRD, FT-IR and UV-vis properties of MgO films," *Physica B Condens Matter*, vol. 570, pp. 280–284, 2019, doi: https://doi.org/10.1016/j.physb.2019.06.020.

[46] M.N. Mirzayev, R.N. Mehdiyeva, R.G. Garibov, N.A. Ismayilova, and S.H. Jabarov, "Influence of gamma irradiation on the surface morphology, XRD and thermophysical properties of silicide hexoboride," *Modern Physics Letters B*, vol. 32, no. 14, p. 1850151, 2018, doi: 10.1142/S0217984918501518.

[47] S.K. Sen, T.C. Paul, S. Dutta, M.N. Hossain, and M. N.H. Mia, "XRD peak profile and optical properties analysis of Ag-doped h-$MoO_3$ nanorods synthesized via hydrothermal method," *Journal of Materials Science: Materials in Electronics*, vol. 31, no. 2, pp. 1768–1786, 2020, doi: 10.1007/s10854-019-02694-y.

[48] J.P. Kollender, A.I. Mardare, and A.W. Hassel, "Effect of Different Cobalt Concentrations on Tungsten Trioxide Photoelectrodes for Use in Solar Water Oxidation," *J Electrochem Soc*, vol. 162, no. 4, pp. H187–H193, 2015, doi: 10.1149/2.0711503jes.

[49] L. Zhang et al., "Recent progress for silver nanowires conducting film for flexible electronics," *J Nanostructure Chem*, vol. 11, no. 3, pp. 323–341, 2021, doi: 10.1007/s40097-021-00436-3.

[50] Shreya, P. Phogat, R. Jha, and S. Singh, "Elevated Refractive Index of $MoS_2$ Amorphous Nanoparticles with a Reduced Band Gap Applicable for Optoelectronics," pp. 431–439, 2023, doi: 10.1007/978-981-99-2349-6_39.

[51] D. Sánchez-Martínez, A. Martínez-De La Cruz, and E. López-Cuéllar, "Synthesis of $WO_3$ nanoparticles by citric acid-assisted precipitation and evaluation of their photocatalytic properties," *Mater Res Bull*, vol. 48, no. 2, pp. 691–697, Feb. 2013, doi: 10.1016/J.MATERRESBULL.2012.11.024.

[52] D. Meng, T. Yamazaki, Y. Shen, Z. Liu, and T. Kikuta, "Preparation of $WO_3$ nanoparticles and application to NO2 sensor," *Appl Surf Sci*, vol. 256, no. 4, pp. 1050–1053, Nov. 2009, doi: 10.1016/J.APSUSC.2009.05.075.

[53] D. Kumari, S. Sharma, P. Phogat, D. Dipti, S. Singh, and R. Jha, "Enhanced electrochemical behavior of C@CdS Core-Shell heterostructures," *Materials Science and Engineering B*, vol. 301, Mar. 2024, doi: 10.1016/j.mseb.2024.117212.

[54] T. Kumar, Shreya, P. Phogat, V. Sahgal, and R. Jha, "Surfactant-mediated modulation of morphology and charge transfer dynamics in tungsten oxide nanoparticles," *Phys Scr*, vol. 98, no. 8, Aug. 2023, doi: 10.1088/1402-4896/ACE566.

[55] Y. Yin, C. Lan, H. Guo, and C. Li, "Reactive Sputter Deposition of $WO_3$/Ag/$WO_3$ Film for Indium Tin Oxide (ITO)-Free Electrochromic Devices," *ACS Appl Mater Interfaces*, vol. 8, no. 6, pp. 3861–3867, Feb. 2016, doi: 10.1021/acsami.5b10665.

[56] P. Phogat, Shreya, R. Jha, and S. Singh, "Diffusion Controlled Features of Microwave Assisted ZnS/ZnO Nanocomposite with Reduced Band Gap," *ECS Journal of Solid State Science and Technology*, vol. 12, no. 3, p. 034004, Mar. 2023, doi: 10.1149/2162-8777/ACC426.

[57] M. Takagi, M. Kawaguchi, and A. Yamakata, "Enhancement of UV-responsive photocatalysts aided by visible-light responsive photocatalysts: Role of $WO_3$ for $H_2$ evolution on CuCl," *Appl Catal B*, vol. 263, p. 118333, 2020, doi: https://doi.org/10.1016/j.apcatb.2019.118333.

[58] O. Gonzalez, T.G. Welearegay, X. Vilanova, and E. Llobet, "Using the Transient Response of $WO_3$ Nanoneedles under Pulsed UV Light in the Detection of $NH_3$ and $NO_2$," *Sensors*, vol. 18, no. 5, 2018, doi: 10.3390/s18051346.

[59] C.C. Mardare and A.W. Hassel, "Review on the Versatility of Tungsten Oxide Coatings," *Physica Status Solidi (A) Applications and Materials Science*, vol. 216, no. 12, Jun. 2019, doi: 10.1002/pssa.201900047.

[60] P.V.K. Yadav, Y.A.K. Reddy, B. Ajitha, and V.R. Minnam Reddy, "Oxygen partial pressure dependent UV photodetector performance of $WO_3$ sputtered thin films," *J Alloys Compd*, vol. 816, p. 152565, 2020, doi: https://doi.org/10.1016/j.jallcom.2019.152565.

[61] B. Bouchikhi et al., "Formaldehyde detection with chemical gas sensors based on $WO_3$ nanowires decorated with metal nanoparticles under dark conditions and UV light irradiation," *Sens Actuators B Chem*, vol. 320, p. 128331, 2020, doi: https://doi.org/10.1016/j.snb.2020.128331.

[62] L. Santos et al., "Synthesis of $WO_3$ nanoparticles for biosensing applications," *Sens Actuators B Chem*, vol. 223, pp. 186–194, Feb. 2016, doi: 10.1016/j.snb.2015.09.046.

[63] Dipti, P. Phogat, Shreya, D. Kumari, and S. Singh, "Fabrication of tunable band gap carbon based zinc nanocomposites for enhanced capacitive behaviour," *Phys Scr*, vol. 98, no. 9, Sep. 2023, doi: 10.1088/1402-4896/ACF07B.

[64] A.C. Anithaa, N. Lavanya, K. Asokan, and C. Sekar, "$WO_3$ nanoparticles based direct electrochemical dopamine sensor in the presence of ascorbic acid," *Electrochim Acta*, vol. 167, pp. 294–302, Jun. 2015, doi: 10.1016/j.electacta.2015.03.160.

[65] P. PHOGAT, . S., R. JHA, and S. Singh, "Electrochemical Analysis of Thermally Treated Two Dimensional Zinc Sulphide Hexagonal Nano-Sheets with Reduced Band Gap," *Phys Scr*, Dec. 2023, doi: 10.1088/1402-4896/AD0D93.

[66] K. Yoon, S. Kim, J.J. Han, S. Han, and M. Preda, "Standard Interfacing Format for Actuators and Sensors," *MPEG-V*, pp. 57–87, 2015, doi: 10.1016/B978-0-12-420140-8.00003-2.

[67] S. Sharma, P. Phogat, R. Jha, and S. Singh, "Enhanced Electrochemical Performance and Charge-Transfer Dynamics of 2D $MoS_2$/$WO_3$ Nanocomposites for Futuristic Energy Applications," *ACS Appl Nano Mater*, Apr. 2024, doi: 10.1021/acsanm.3c06017.

[68] A. Sharma, S. Sharma, P. Phogat, R. Jha, and S. Singh, "Hydrothermally Synthesized $NiS_2$ and $NiSO_4(H_2O)_6$ Nanocomposites and its Characterizations," *MATEC Web of Conferences*, vol. 393, Mar. 2024, doi: 10.1051/matecconf/202439301016.

[69] S. Rai, S. Sharma, P. Phogat, R. Jha, and S. Singh, "Hydrothermal synthesis and characterization of selenium-doped $MoS_2$ for enhanced optoelectronic properties," *MATEC Web of Conferences*, vol. 393, Mar. 2024, doi: 10.1051/matecconf/202439301008.

[70] S. Sharma, P. Phogat, S. Singh, and R. Jha, "Reduction mechanism of hydrothermally synthesized wide band gap ZnWO4 nanorods for HER application," *MATEC Web of Conferences*, vol. 393, Apr. 2024, doi: 10.1051/matecconf/202439301004.

[71] A. K. Thakur et al., "Controlled synthesis of $WO_3$ nanostructures: optical, structural and electrochemical properties," *Mater Res Express*, vol. 6, no. 2, p. 25006, Nov. 2018, doi: 10.1088/2053-1591/aae991.

[72] I. Aslam et al., "Synthesis of $WO_3 \cdot H_2O$ spherical particles for efficient photocatalytic properties under visible light source," *Mater Sci Energy Technol*, vol. 2,

no. 2, pp. 187–193, 2019, doi: https://doi.org/10.1016/j.mset.2019.02.002.

[73] U. T. Nakate, V. K. Singh, Y. T. Yu, and S. Park, "$WO_3$ nanorods structures for high-performance gas sensing application," *Mater Lett*, vol. 299, p. 130092, 2021, doi: https://doi.org/10.1016/j.matlet.2021.130092.

[74] C. Kamble, M. Panse, and A. Nimbalkar, "Ag decorated $WO_3$ sensor for the detection of sub-ppm level $NO_2$ concentration in air," *Mater Sci Semicond Process*, vol. 103, p. 104613, 2019, doi: https://doi.org/10.1016/j.mssp.2019.104613.

[75] P. Phogat, S. Sharma, R. Jha, and S. Singh, "Phase Transition of Thermally Treated Polyhedral Nano Nickel Oxide with Reduced Band Gap," *MATEC Web of Conferences*, vol. 393, Apr. 2024, doi: 10.1051/matecconf/202439301001.

[76] A. Rai, P. Phogat, S. Sharma, R. Jha, and S. Singh, "Microwave Assisted Zinc Sulphide Quantum Dots for Energy Device Applications," *MATEC Web of Conferences*, vol. 393, Mar. 2024, doi: 10.1051/matecconf/202439301011.

[77] H. Koohestani, "Characterization of TiO2/$WO_3$ composite produced with recycled WO3 nanoparticles from WNiFe alloy," *Mater Chem Phys*, vol. 229, pp. 251–256, 2019, doi: https://doi.org/10.1016/j.matchemphys.2019.03.027.

[78] A.-Z. Warsi, F. Aziz, S. Zulfiqar, S. Haider, I. Shakir, and P.O. Agboola, "Synthesis, Characterization, Photocatalysis, and Antibacterial Study of $WO_3$, MXene and $WO_3$/MXene Nanocomposite," *Nanomaterials*, vol. 12, no. 4, 2022, doi: 10.3390/nano12040713.

[79] M. Rakibuddin and H. Kim, "Synthesis and characterization of facile industrially scalable and cost effective $WO_3$ micro–nanostructures for electrochromic devices and photocatalyst," *Ceram Int*, vol. 44, no. 14, pp. 16615–16623, 2018, doi: https://doi.org/10.1016/j.ceramint.2018.06.088.